

Incorporation of thorium in the zircon structure type through the Th_{1-x}Er_x(SiO₄)_{1-x}(PO₄)_x thorite-xenotime solid solution

Mesbah, A.; Clavier, N.; Lozano-Rodriguez, J.; Szenknect, S.; Dacheux, N.;

Originally published:

October 2016

Inorganic Chemistry 55(2016)21, 11273-11282

DOI: <https://doi.org/10.1021/acs.inorgchem.6b01862>

Perma-Link to Publication Repository of HZDR:

<https://www.hzdr.de/publications/Publ-24041>

Release of the secondary publication
on the basis of the German Copyright Law § 38 Section 4.

This document is confidential and is proprietary to the American Chemical Society and its authors. Do not copy or disclose without written permission. If you have received this item in error, notify the sender and delete all copies.

**Incorporation of thorium in the zircon structure type
through the $\text{Th}_{1-x}\text{Er}_x(\text{SiO}_4)_{1-x}(\text{PO}_4)_x$ thorite-xenotime
solid solution**

Journal:	<i>Inorganic Chemistry</i>
Manuscript ID	Draft
Manuscript Type:	Article
Date Submitted by the Author:	n/a
Complete List of Authors:	Mesbah, Adel; Institut de chimie separative de Marcoule, Clavier, Nicolas; ICSM, Lozano-Rodriguez, M. Janeth; Helmholtz Zentrum Dresden Rossendorf, Institute of Resource Ecology Szenknect, Stéphanie; CEA, ICSM Dacheux, Nicolas; ICSM, Bat 426

SCHOLARONE™
Manuscripts

Title: Incorporation of thorium in the zircon structure type through the $\text{Th}_{1-x}\text{Er}_x(\text{SiO}_4)_{1-x}(\text{PO}_4)_x$ thorite-xenotime solid solution

Adel Mesbah,^{†,*} Nicolas Clavier,[†] Janeth Lozano-Rodriguez,[‡] Stephanie Szenknect,[†] Nicolas Dacheux.[†]

[†] ICSM, UMR 5257 CEA / CNRS / ENSCM / University of Montpellier, Site de Marcoule – Bât. 426, BP 17171, 30207 Bagnols-sur-Cèze cedex, France

[‡] HZDR, Institute of Resource Ecology, the Rossendorf Beamline at ESRF, P.O. Box 220, 38043 Grenoble, France

Abstract

Pure powdered compounds with a general formula $\text{Th}_{1-x}\text{Er}_x(\text{SiO}_4)_{1-x}(\text{PO}_4)_x$ belonging to the zircon-xenotime were successfully synthesized under hydrothermal conditions (250°C, 7 days) as recently reported for the preparation of coffinite. Therefore a thorough combined PXRD, EDS, EXAFS, μ -Raman and FTIR analyses showed the formation of solid solution in agreement with the Vergard's law. Moreover, the examination of the local structure shows that the Th-O distances remain close to those found in ThSiO_4 . Whereas, the Er-O distances show big decrease from 2.38(14) Å to 2.34(7) Å when increasing the erbium content from $x = 0.2$ to $x = 1$. The variation of the local structure also affects the PO_4^{3-} groups that are surely distorted in the structure.

1. INTRODUCTION

The crystal chemistry of lanthanides phosphates ($\text{Ln}^{\text{III}}\text{PO}_4$) and actinides silicates ($\text{An}^{\text{IV}}\text{SiO}_4$) is governed, at high temperature, by the existence of two distinct structural types. On the one hand, the monazite structure (monoclinic, space group $P2_1/n$)¹ is generally the most stable phase for light rare earth elements (REE) phosphates (typically from La to Gd) and was also reported for ThSiO_4 (corresponding to the mineral huttonite)^{2,3} and PaSiO_4 .⁴ The original MO_9 coordination polyhedron encountered in the monazite confers to the structure the capability to incorporate a wide range of elements through direct and/or coupled substitutions, either on the cationic or the anionic site⁵, leading to a tremendous variety of applications. On the other hand, heavy REE phosphates (namely from TbPO_4 to LuPO_4) which relate to the mineral xenotime, and all tetravalent actinides phosphates (including ThSiO_4 thorite⁶, USiO_4 coffinite^{7,8} and associated solid solutions⁹⁻¹²) preferentially adopt the zircon-type structure in the tetragonal system with $I4_1/amd$ as a space group. Silicate-based compounds of this family then also include zircon (ZrSiO_4) and hafnon (HfSiO_4).

Monazite, xenotime and zircon are widespread naturally occurring minerals.¹³⁻¹⁸ They coexist in many granitic and metamorphic rocks located in different sites on earth¹⁹⁻²³ and exhibit a very rich structural diversity owing to their ability to contain a wide variety of rare earth elements (REE) and natural actinides (U and Th). Indeed, these three minerals represent the main sources of the REE, U and Th on earth, with monazite being considered as the first source of thorium and coffinite as the second source of tetravalent uranium after uraninite.¹³ Many works already demonstrated the utility of the presence of the actinides and associated daughter products (U-Th-Pb) for the precise dating of the rocks in the field of geochronology.²⁴⁻³² Moreover, the distribution of REE between the monazite and xenotime minerals, which depends on the temperature of formation, led these phases to be used as geothermobarometer leading to the determination of the history of the related metamorphic rocks.^{21,33} More importantly, these minerals have attracted many interests in the industrial field linked to the nuclear fuel cycle, whether as uranium and thorium sources (front-end) or as specific ceramics for the conditioning of highly radioactive nuclear wastes (back-end).^{13,34-41} They were also proposed for the disposal of excess plutonium coming from the dismantlement of nuclear weapons⁴². For both purpose, monazite and zircon were generally associated to remarkable properties, such as high resistance

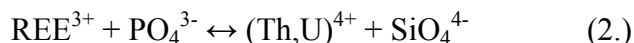
to aqueous leaching and radiation damages. Additionally, zircon was frequently cited as a promising inert matrix for the transmutation of minor actinides (particularly Np, Am and Cm) in fast-neutron reactors or accelerator-driven systems.⁴³

From a structural point of view, uranium and thorium are incorporated in both monazite and xenotime structures following various substitution mechanisms. The most encountered case consists of the miscibility between the monazite (REEPO₄) and the cheralite (CaAn(PO₄)₂) through



as observed in natural minerals by Foster⁴⁴ and confirmed on synthetic compounds.^{39,45} Another possibility of substitution consists of the formation of solid solutions between the monazite and isostructural ThSiO₄ huttonite. Such samples were both reported to exist in natural phases⁴⁶ and prepared as synthetic compounds, either through hydrothermal wet chemistry methods⁴⁷ or dry chemistry routes, leading to complex compositions such as the Ln_{0.7}Th_{0.27}U_{0.03}(PO₄)_{0.7}(SiO₄)_{0.3} reported by McCarthy *et al.*⁴⁸

In the case of the presence of Y³⁺ or heavy REE, xenotime became the stable phase. According to literature, thorium and uranium could then only be incorporated through:



Although both xenotime and zircon compounds are crystallizing in the same structure type, there is no accurate study dedicated to the existence of solid solution between both end members.^{28,49,50} In the latter works, all the attempts to synthesize solid solution between xenotime and zircon have been carried out by solid state chemistry (flux method) and only led to the partial insertion of PO₄³⁻ and REE³⁺ in the ZrSiO₄ structure type and vice versa.

In this present paper, we thus report the first synthesis of a complete solid solution Th_{1-x}Er_x(SiO₄)_{1-x}(PO₄)_x (with 0 ≤ x ≤ 1, by steps of 0.1) in the thorite – xenotime system. Thorium was selected as a model element for tetravalent actinides, which avoided any perturbations due to redox reactions. Also, erbium was considered as the rare earth element due to its use as a burnable poison in inert matrix fuels, which controls the reactivity towards irradiation.^{51,52} All the compounds prepared were thoroughly characterized from a structural point of view by PXRD and EXAFS. Vibrational spectroscopy features were also investigated by Raman and FTIR.

2. MATERIALS AND METHODS

Caution! Depleted uranium and ^{232}Th are α - emitters and are considered as a health risk. Experiments involving actinides requires appropriate facilities and trained persons in handling of radioactive materials.

Synthesis. For the synthesis of the $\text{Th}_{1-x}\text{Er}_x(\text{SiO}_4)_{1-x}(\text{PO}_4)_x$ solid solutions, the following reactants were used: $\text{Th}(\text{NO}_3)_4 \cdot 4\text{-}5\text{H}_2\text{O}$, $\text{ErCl}_3 \cdot n\text{H}_2\text{O}$, NaOH , NaHCO_3 , Na_2SiO_3 . All chemicals were of analytical grade and supplied by Sigma-Aldrich. Precise and direct weighing of the exact amounts of thorium and erbium salts was precluded because of their hygroscopic character. Therefore, both salts were dissolved in acidic media. ErCl_3 was dissolved in 1M HCl while the thorium chloride concentrated solution was prepared by dissolving thorium nitrate pentahydrate in concentrated HCl solution. Several cycles of evaporation and re-dissolution in a solution of 4M HCl were undertaken until traces of nitrates were eliminated.⁵³ Concentrations of resulting solutions were finally determined by ICP-AES using a Spectro Arcos EOP device. The calibration of the apparatus was performed by the means of SPEX standard solutions diluted to concentrations varying between 0 and 15 mg.L^{-1} .

Powder X-Ray Diffraction (PXRD). The synthesized compounds were analyzed by PXRD with the help of Bruker D8 advance diffractometer equipped with the Lynxeye detector and $\text{Cu K}_{\alpha 1,2}$ radiation ($\lambda=1.54184 \text{ \AA}$). The measurements were carried out in parallel geometry and using adapted sample holders (dome) in order to prevent from any radioactive contamination. Each powder XRD pattern was collected in the angular range (2θ) between 5 and 100° with a step of 0.019° and a total counting time of about 3 hours per sample. Also, a PXRD pattern of pure silicon powder was collected in similar conditions in order to evaluate the instrumental function. In all cases only the zircon structure type⁵⁴ ($I4_1/amd$ space group) was the detected phase. Therefore, all the collected data were refined by the Rietveld method using the Fullprof_suite package.⁵⁵ During the refinements, different profile and structure parameters were allowed to vary such as: the zero shift, unit cell parameters, scale factor, overall displacement factor.

Moreover, an anisotropic size model was applied in order to evaluate the peaks broadening due to microstructural effect. However, the occupancy of each site was fixed to the calculated values.

Extended X-ray Absorption Fine Structure. EXAFS measurements were performed in transmission mode at the Th L₃-edge (16300 eV) and the Er L₃-edge (8358 eV) of ten Th_{1-x}Er_x(SiO₄)_{1-x}(PO₄)_x samples (x=0, 0.2, 0.3, 0.4, 0.5, 0.6, 0.7, 0.8, 0.9 and 1) mixed with boron nitride (BN). The measurements were carried out at the Rossendorf Beamline (BM20) dedicated to actinides based compounds, located at the European Synchrotron Radiation Facility (ESRF; Grenoble, France). The storage ring operated at 6 GeV and 170-200 mA. For the Th L₃-edge, a double Si (111) 30° crystal monochromator was used for energy selection, and a pair of Rh mirrors were used for vertical beam collimation and suppression of higher-order harmonics. A gas mixture of 80% N₂ and 20% Ar was used in the 30-cm ionization chamber measuring the incoming beam (I₀) and 100% Ar gas was used to measure the beam transmitted through the sample (I₁) and after the respective reference foil (I₂), all filled at ambient pressure. While for Er L₃-edge, a double Si (111) 0° crystal monochromator was used for energy selection combined with a pair of Si/Rh mirrors. Likewise, a gas mixture of 70% He and 30% N₂ was used in the ionization chamber. Energy calibration was done by measuring the absorption spectra of Y (17038 eV) and Ni (8333 eV) metal foils placed between I₁ and I₂ parallel to the sample scans. All the samples were measured at room temperature.

Data reduction and extraction of EXAFS oscillation was performed using the Athena and Artemis package.⁵⁶ The threshold energy, E₀, was defined as the maximum of the first derivative of the absorption coefficient. Experimental EXAFS spectra were Fourier transformed using a Hanning window over the k-space ranges of 2-11 Å⁻¹ for thorium and 2.5-11 Å⁻¹ for erbium. The shell fits were performed in R-space using k^1 , k^2 and k^3 -weighted for thorium and erbium. Theoretical phase shifts and backscattering amplitudes were obtained with the ab initio code FEFF8.2⁵⁷ using the ThSiO₄ (thorite)² and ErPO₄ (xenotime) structures¹⁴ for thorium and erbium L₃-edge reported in the literature. The calculation was carried out with a radius cluster of 6 Å, taking into account all single scattering (SS) and multiple scattering (MS). During the fitting procedure, Th-O, Th--Si₁ (P₂), Th -- Si₂ (P₂) and Th-Th (Er) single scattering paths (SS) were taken into account. Similarly, Er-O, Er--P₁ (Si₁), Er--P₂ (Si₂) and Er-Er (Th) SS were considering

for the fitting. The distances (R) and Debye-Waller (DW) factors were treated as free parameters, while the coordination number (N) were constrained at crystallographic values. A single shift in the threshold energy (ΔE_0) for each composition was varied as a global parameter. The amplitude reduction factor S_0^2 was obtained for ThSiO_4 and for ErPO_4 after keeping the obtained value constant through the whole compositions. To assure transferability of phase and amplitude and to allow the estimation of systematic errors, all the data were analyzed using the same experimental phases and amplitude, filtering procedures and parameters in a similar way.

Scanning Electron Microscopy. SEM observations were directly conducted on powdered samples without any preparation such as metallization, using a Tescan Vega3 electronic microscope, in low vacuum conditions (10 Pa) with an accelerating voltage of 15 kV. Additionally, the precise chemical composition of the series $\text{Th}_{1-x}\text{Er}_x(\text{SiO}_4)_{1-x}(\text{PO}_4)_x$ was analyzed by the means of Energy Dispersive Spectrometry (EDS) coupled with a FEI Quanta 200 SEM device. In this aim, the powder was first embedded in an epoxy resin. The surface of the sample was then polished to reach an optical grade and metalized by carbon coating. Experimental data were finally collected from about 50 different locations of the sample surface, considering ThO_2 and ErPO_4 as internal standards.

Vibrational spectroscopy. Raman spectra were recorded in the $100\text{-}1500\text{ cm}^{-1}$ range by the means of a Horiba - Jobin Yvon Aramis apparatus equipped with an edge filter and using a He-Ne laser (633 nm) delivering 10 mW on the sample surface. The laser beam was then focused on a small fraction of powdered sample simply deposited on a glass lamella using an Olympus BX 41 microscope. The scattered Raman light was collected in a 180° backscattering geometry and dispersed by a grating of 1800 grooves/mm after having passed a $150\text{ }\mu\text{m}$ entrance slit, resulting in a spectral resolution lower than 1 cm^{-1} . For each spectrum, a dwell time of 30 seconds was considered with an average of 10 scans. Before analysis, the apparatus was calibrated with a silicon wafer, using the first-order Si line at 520.7 cm^{-1} .

FTIR spectra were recorded in the $380\text{-}4000\text{ cm}^{-1}$ range thanks to a Perkin-Elmer FTIR Spectrum 100 device. Powdered samples were deposited at the surface of an ATR crystal without any prior preparation. The spectra collected in such operating conditions exhibited a resolution lower than 2 cm^{-1} .

3. RESULTS AND DISCUSSION

3.1 Synthesis and SEM/EDX characterization

First attempts to prepare $\text{Th}_{1-x}\text{Er}_x(\text{SiO}_4)_{1-x}(\text{PO}_4)_x$ solid solutions were performed by following several methods previously reported in the literature for the synthesis of rhabdophane or xenotime-type compounds.⁵⁸ The first protocol considered consisted of the direct coprecipitation of the reactants in aqueous solution. A starting mixture of thorium and erbium in the desired stoichiometric ratio was then poured in a solution containing 5M H_3PO_4 and dissolved Na_2SiO_3 then transferred in a Teflon container at 90°C for 2 weeks. Nevertheless, the PXRD patterns analysis of the resulting powder (not presented here) showed the formation of an amorphous gel whatever the chemical composition considered. The second method consisted of a heat treatment of the previous mixtures at 250°C. However, this chemical route also failed yielding to a polyphase system composed mainly of thorite (ThSiO_4) and Er-xenotime (ErPO_4).

Finally, powdered samples of $\text{Th}_{1-x}\text{Er}_x(\text{SiO}_4)_{1-x}(\text{PO}_4)_x$ solid solutions were prepared by using a method recently reported in the literature for the synthesis of coffinite USiO_4 ⁵⁹, in modification of the protocol initially proposed by Hoekstra and Fuchs.⁸ The calculated amount of Na_2SiO_3 was dissolved in deionized water and mixed with desired amount of 5M H_3PO_4 . In parallel, weighed amounts of Th and Er acidic solutions were mixed and then poured slowly into the anionic solution under continuous stirring. Then the pH of the solution was raised by adding dropwise 8M NaOH to the target value ranging between 11 and 11.5. Afterwards, the solution was buffered to 8.7 ± 0.1 by adding NaHCO_3 . The final solution was transferred into a teflon-lined acid digestion bomb (Parr) and placed in an oven for one week at 250 °C. All the reactions were carried out in fume hood in air. The precipitate collected after this treatment was separated from the supernatant by centrifugation at 4500 rpm, washed twice with deionised water and ethanol, then finally dried overnight at 90°C.

For all the sample compositions studied, the powders were found to consist of small needle-like crystals. The size of these grains was typically in the 200-800 nm range but no clear trend was established versus the erbium weight loading, Figure 1 shows selected micrographs of four different compositions. The analysis of the synthesized powders by EDX confirmed the formation of samples with the presence of Th, Er, Si and P within the structure. The trend of the measured values confirms the formation of solid solution as shown in Table 1. Regarding the results reported, we observe a small and systematic deviation of the measured values compared to the calculated ones but still acceptable as experimental errors. The values obtained for the phosphorus values with a systematic miss estimation of about 5% of P atomic percentage. This problem is a recurrent one on all our phosphate based compounds which is mainly due a bias caused by the standardization method. Moreover, attempts to perform a total dissolution in aqua regia of the powders were unsuccessful because of the precipitation of amorphous silica which made difficult the collection of reliable data.

3.3 Structural characterization

PXRD. All the powdered samples prepared were analyzed by PXRD (Figure 2a). Systematically, only the zircon structure type was observed, conversely to the case of uranorthorite ($\text{Th}_{1-x}\text{U}_x\text{SiO}_4$),^{10,11} which led to the formation of mixed phases with the simultaneous stabilization of nanometric $\text{Th}_{1-y}\text{U}_y\text{O}_2$ and SiO_2 byproducts. Given those results, the reactions performed under hydrothermal conditions at 250°C have led to the formation of a single pure phase crystallizing in the zircon structure type which corresponds to the expected $\text{Th}_{1-x}\text{Er}_x(\text{SiO}_4)_{1-x}(\text{PO}_4)_x$ solid solution. All these compounds crystallize in the tetragonal system, with a space group of $I4_1/amd$ (general view of the structure down the c axis presented in Figure 3). In this system, both end-members, namely ThSiO_4 ^{2,60} and ErPO_4 ⁶¹, are well known and isostructural but generally differ in their way of synthesis.

The analysis of the patterns reported in Figure 2a evidenced a shift in the XRD lines toward the low angles (2θ) depending on the erbium content. The experimental unit cell parameters, refined using Rietveld methods, are reported in Table 2 while Figure 2b shows the observed, calculated

and the difference curves for the compound $\text{Th}_{0.5}\text{Er}_{0.5}(\text{SiO}_4)_{0.5}(\text{PO}_4)_{0.5}$ refined in the zircon structure type. Moreover, the linear variation of the unit cell volume versus the erbium content, viewed in Figure 4, appears in agreement with the Vegard's law. At first glance, this variation appears to be in agreement with crystal ionic radius reported in the Shannon tables for Th^{4+} and Er^{3+} in coordination eight with $r = 1.19 \text{ \AA}$ and 1.144 \AA , respectively. Moreover, we should also consider the size of Si^{4+} (0.4 \AA) and P^{5+} (0.3 \AA) in the structure. From the microscopic point of view, it seems that the formed solid solution exhibits a perfectly random distribution between the elements in both sites Th/Er and Si/P inside the structure. In order to obtain more information and details EXAFS experiments were performed to probe the local structure as detailed below.

Local structure. To clarify the behavior of erbium and its influence on the host ThSiO_4 , the local structure of thorium and erbium in all the $\text{Th}_{1-x}\text{Er}_x(\text{SiO}_4)_{1-x}(\text{PO}_4)_x$ samples prepared were systematically investigated by EXAFS at Th and Er L_3 -edges. The k^3 -weighted EXAFS spectra and their Fourier Transform (FTs) obtained for the ten different compositions are shown in Figure 5a and 5b for the Th and Er L_3 -edges, respectively.

The FT obtained for the ThSiO_4 end-member ($x=0$) at the Th L_3 -edge shows a first shell around the thorium atom consisting of eight oxygen contributions at 2.4 \AA . The next neighbor contributions at 3.20 \AA and 3.95 \AA were attributed to the single scattering contribution of two Si_1 and four Si_2 atoms in the thorite structure, respectively. Additionally, a cation-cation contribution related to the Th—Th was fitted at 3.93 \AA . Besides, the FT determined for ErPO_4 ($x=1$) at Er L_3 -edge (Figure 5b) also shows the eight oxygen contributions in the first coordination shell at 2.34 \AA . In the same way that for ThSiO_4 , the FT of ErPO_4 presents a second and a third peak related to the single scattering contribution of two P_1 at 3.03 \AA and four P_2 at 3.88 \AA . For the ErPO_4 end-member, it was also possible to fit two Er—Er distances, at 3.76 \AA and 5.69 \AA . For the rest of the compositions, the longest Er contribution was no longer observable. These values are shown in the Table 3 and were found to be in agreement with the average crystal diffraction distances reported in the literature.^{2,14,60}

For intermediate solid solutions, the FT measurements at Th L_3 -edge from $x=0$ to $x=0.5$ (Figure 5a) showed little changes on the local environment around Th. However, starting from $x=0.5$ to $x=0.8$, the amplitude of Th peak contribution decreased whereas a broadening on the Si_2 peaks

was revealed. Such behavior might be related to the shortening of Th—Th(Er) distances as actinide content decreased and/or to interferences between the two Er and Th scattering paths resulting in the attenuation of the cation-cation FT peak. The EXAFS spectra for the Th L₃-edge showed no modification at lower *k*-ranges. However, small modifications started at 8 Å⁻¹ probably due to the mixing backscattering between Th and Si atoms. Conversely, the FTs of Th_{1-x}Er_x(SiO₄)_{1-x}(PO₄)_x solid solutions at Er L₃-edge (figure 5b) showed more significant changes in the local environment around Er than those of Th L₃-edge at higher Er content (x=0.9). Such modifications were also revealed in their EXAFS spectra, where a bigger change in the atomic structure around the xenotime ErPO₄ was observed as Th content increased.

Cation oxygen environment. According to the criteria for isovalent solid solutions, the bond length could be limited by two cases, which will reflect their ability to adapt to the host structure. The first is a *no relaxation* in the system, which assumes that the atomic radii are approximately conserved and independent of the composition of the solid solution (Pauling's concept). In contrast, the second corresponds to a *full relaxation* in the system, where the virtual crystal approximation (VCA) is valid and bond lengths follow Vegard's law.⁶²

The cation-oxygen interatomic distances are presented in Figure 6, with respective error bars calculated from the difference of EXAFS values and the distances of the crystal structure mentioned already. The derived Th-O and Er-O bond length distances showed that Th-O and Er-O distances are element-specific due to the difference in their crystal effective radius (1.144 Å for Er and 1.19 Å for Th). The Er-O bond length determined by EXAFS increased in the zircon-type structure with the thorium content. However, the individual Th-O bond length remained close to the value determined in pure ThSiO₄ (2.39 Å), i.e. that there is no relaxation. It suggests that Th-O bond lengths are preserved in the first coordination shell as erbium content increases, due to its strong covalent bond. From these results, the host zircon-type structure (ErPO₄) is modified with the change in the actinide content (i.e. full relaxation).⁶³ Besides, the average EXAFS distance plotted in figure 6 showed a similar trend compared to PXRD results (Figure 4). Another observation is that the Debye-Waller factor (σ^2) in the Er-O coordination shell is increasing with thorium content, going from 0.0550 to 0.0100 Å². However, the σ^2 values for Th-

O contribution remained at the same scale, with an average of 0.006 \AA^2 in average. Note that this reflects the thermal and static contribution since measurements were performed at room temperature.

Cation-cation environment. The cation-cation distribution was determined with a single broad peak within the EXAFS resolution. The variation in the second neighbor distribution is presented in Figure 7 with corresponding error bars. First, the Er-Er (Th) and Th-Th (Er) distances are approximatively equal to their average distances, as reported previously in the case of covalent and ionic systems.^{63,64} Secondly, looking at the Er-Er (Th) local environment, a change from 3.76 \AA to 3.94 \AA was observed. Nonetheless, the Th-Th (Er) local environment suffered a small variation from 3.93 \AA to 3.90 \AA . These results again suggest that, although the Er local structure was modified, that of Th remained close to pure thorite (ThSiO_4). This kind of behavior was already reported for stabilized zirconia with actinides.^{65,66} In addition, as the thorium content increased, the Er-Er (Th) bond length distances became similar to the Th-Th ones. Finally, Figure 8 shows the variation in the Er—P and Th—Si interatomic distances. It is important to mention that P and Si are undistinguishable by EXAFS because of their close atomic number. However, from fitting, it was observed that Th-Si and Er-P distances remained almost constant, meaning that there is a less significant change in their distances than those obtained for the cations.

3.5 Vibrational spectroscopy

The vibrational features of XO_4 anions within a zircon-type structure have been widely described, either in the case of phosphate species for the xenotime⁶⁷, or for silicates in actinide-based compounds such as thorite⁶⁸ or coffinite⁹. The factor group analysis based on the irreducible representation of the D_{4h} point group leads to the optical vibrations as follows:

$$\Gamma = 2A_{1g} + 2A_{2g} + 4B_{1g} + B_{2g} + 5E_g + A_{1u} + 3A_{2u} + B_{1u} + 2B_{2u} + 4E_u \quad (1.)$$

Among these vibration modes, 12 are Raman-active and split between the 7 internal vibrations of the XO_4 tetrahedra (Γ_{int}) and 5 external modes corresponding to the motion of solid tetrahedral in the unit cell (Γ_{ext}), such as :

$$\Gamma_{\text{int}} = 2A_{1g} + 2B_{1g} + B_{2g} + 2E_g \quad (2.)$$

$$\Gamma_{\text{ext}} = 2B_{1g} + 3E_g \quad (3.)$$

Similarly, FTIR-active vibration modes can be described as :

$$\Gamma_{\text{int}} = A_{1u} + 2A_{2u} + 2B_{2u} + 2E_u \quad (4.)$$

$$\Gamma_{\text{ext}} = A_{2u} + B_{1u} + 2E_u \quad (5.)$$

The Raman spectra recorded for the $\text{Th}_{1-x}\text{Er}_x(\text{SiO}_4)_{1-x}(\text{PO}_4)_x$ solid solutions generally appeared in good agreement with this factor-group analysis (Figure 9). For the ErPO_4 end-member, the 7 vibration modes of the phosphate tetrahedra (numbered after the nomenclature employed by Kolesov *et al.*⁶⁹) were observed at 334 and 473 cm^{-1} (ν_2 : symmetric bending), 590 and 665 cm^{-1} (ν_4 : antisymmetric bending), 999 cm^{-1} (ν_1 : symmetric stretching) and 1021 and 1057 cm^{-1} (ν_3 : antisymmetric stretching), along with the rotational external vibration at 296 cm^{-1} . These results match the previous works undertaken on Er-based xenotime^{67,70}, although the position of the vibration bands appears to be slightly modified, probably due to the presence of interference bands between 400 and 850 cm^{-1} . This rogue signal corresponds to the red luminescence emission of Er^{3+} at 652 nm, from the $^4F_{9/2} \rightarrow ^4I_{15/2}$ transition^{71,72}. On the other hand, only 4 internal vibration modes of the silicate group were observed in the thorite end-member, at 438 (ν_2), 592 (ν_4), 887 (ν_1) and 914 cm^{-1} (ν_3). Nevertheless, such discrepancy was already reported by several authors and correlated to the existence of interactions between SiO_4 tetrahedra and the metallic cation⁶⁸. In this case, silicates unit cannot be treated strictly independently, resulting in less internal vibration modes than predicted by the factor-group analysis.

Between these two extreme cases, the Raman spectra recorded for the xenotime-thorite solid solutions exhibit the vibrational features of both structures, although with notable variations in their relative intensities. Indeed, the modes related to silicate units rapidly vanished when decreasing the thorium content in the sample, and were almost undetectable for $x < 0.7$. This phenomenon probably arose from the better answer of phosphate tetrahedra in Raman spectroscopy, but also from the progressive incorporation of erbium in the sample which induced an increasing parasite emission in the $\nu_2(\text{SiO}_4)$ and $\nu_4(\text{SiO}_4)$ zone. Same applies for the PO_4 bending mode in this region of the spectra. Conversely, it appeared easier to follow the variation of the phosphate stretching modes which remained visible whatever the thorium incorporation rate (x). On this basis, the ν_1 vibration band was fitted thanks to the Jandel Peakfit software, using a pseudo-Voigt function with a Gaussian-Lorentzian ratio systematically higher than 0.7. By this mean, correlation coefficients r^2 greater than 0.992 were usually obtained, and led to plot the variation of the ν_1 Raman shift versus x (Figure 10). This latter was found to follow a linear trend, with :

$$\sigma(\nu_1) = 964 + 33 \times x \quad (6.)$$

Such linear variation of the XO_4 stretching mode was already pointed out in the case of cationic substitutions within zircon-type silicates, such as $\text{Zr}_{1-x}\text{Hf}_x\text{SiO}_4$ ⁷³, $\text{Zr}_{1-x}\text{U}_x\text{SiO}_4$ ⁷⁴ and $\text{Th}_{1-x}\text{U}_x\text{SiO}_4$ ⁹. However, it has never been mentioned, to our knowledge, in the case of couple substitutions that involve modifications on both cationic and anionic sites. Moreover, this linear behavior appears in good agreement with the formation of a complete solution between ErPO_4 xenotime and ThSiO_4 thorite. Indeed, with the progressive substitution of Th^{4+} by Er^{3+} , and simultaneously of silicate units by phosphate groups, leading to the shrinkage of the quadratic unit cell, one can expect the P-O bond length to decrease, then an increase in the vibration frequency. Also, one can note that the progressive replacement of erbium by thorium, on the one hand, and of phosphate by silicate, on the other, led the ν_1 vibration band to wider progressively. Since the PXRD study did not evidence any significant influence of the substitution on the crystallization state of the samples, the broadening of the signal might reflect a modification of the PO_4 polyhedra. In these conditions, the phosphate tetrahedrons not only shrink, but are also

probably distorted, leading to the apparition of additional vibration modes overlapping with the initial ν_1 vibration.

These results were confirmed by the data obtained by FTIR spectroscopy (Figure 11), which again exhibited the characteristic vibration modes usually described for xenotime and thorite end-members. Moreover, the better sensitivity of the silicate units to FTIR compared with Raman, as well as the absence of interference luminescence phenomena, offered the possibility to directly compare the modifications in the relative intensities of the SiO_4 and PO_4 stretching modes. Hence, the progressive substitution of the anionic specie along the $\text{Th}_{1-x}\text{Er}_x(\text{SiO}_4)_{1-x}(\text{PO}_4)_x$ solid solution led to the apparition of a crossing point at around 910 cm^{-1} . In this case, vibrational spectroscopy can thus be used to roughly estimate the chemical composition of the solid.

4. CONCLUSION

The incorporation of actinides in potential conditioning matrices such as phosphates or silicates remains a very important point to examine from a chemical point of view. Although several protocols are reported in the literature based on the use of solid-state chemistry methods at high temperature, these methods, do to a lack in the reactivity of the powders or insufficient homogenization during the mixing or grinding steps, often lead to the presence of less durable secondary phases during leaching tests. On the contrary, the development of wet chemistry routes are often considered as promising alternative way to obtain directly the target matrices at lower temperature and with an improve homogeneity. In this purpose, pure powdered compounds $\text{Th}_{1-x}\text{Er}_x(\text{SiO}_4)_{1-x}(\text{PO}_4)_x$ belonging to the zircon-xenotime structure type were successfully synthesized under hydrothermal conditions ($T = 250^\circ\text{C}$, $t = 7$ days) in application of the recent protocol used for the synthesis of the coffinite.⁵⁹ The characterization by SEM (EDS) and PXRD confirmed the formation of a complete solid solution in whole composition range in agreement the Vegard's law. The crystal structure of these solids exhibited a linear decrease of the unit-cell volume as a function of the erbium/phosphate content. However, the analysis of the local structure in particular with EXAFS measurement shows that the Th-O distances do not evolve so much during the erbium to thorium substitution and remain close to those found for the thorite end-member (ThSiO_4). On the contrary, the Er-O-(P,Si) sequence suffers more than Th-O-(P,Si) during the $(\text{Th}, \text{SiO}_4) \Leftrightarrow (\text{Er}, \text{PO}_4)$ substitution, by showing a significant increase of the Er-O distance when increasing the the thorium content in the structure. Correlatively, a distortion of the phosphate groups was observed of spectroscopy.

Acknowledgments

Authors would like to thank C. Gausse, P.H. Imbert and J.M. Sandate Dominguez for their help in the preparation of the samples and EXAFS measurements. They are also grateful to R. Podor for supporting SEM/experiments.

REFERENCES

- (1) Mooney, R. C. L. *Journal of Chemical Physics* **1948**, *16*, 1003.
- (2) Taylor, M.; Ewing, R. C. *Acta Crystallographica Section B-Structural Science* **1978**, *34*, 1074.
- (3) Pabst, A. *Am Mineral* **1951**, *36*, 60.
- (4) Keller, C. *Nukleonik* **1963**, *5*, 41.
- (5) Clavier, N.; Podor, R.; Dacheux, N. *J Eur Ceram Soc* **2011**, *31*, 941.
- (6) Fuchs, L. H. *American Mineralogist* **1958**, *43*, 367.
- (7) Fuchs, L. H.; Gebert, E. *American Mineralogist* **1958**, *43*, 243.
- (8) Hoekstra, H. R.; Fuchs, L. H. *Science* **1956**, *123*, 105.
- (9) Clavier, N.; Szenknect, S.; Costin, D. T.; Mesbah, A.; Poinssot, C.; Dacheux, N. *Spectrochim Acta A* **2014**, *118*, 302.
- (10) Costin, D. T.; Mesbah, A.; Clavier, N.; Szenknect, S.; Dacheux, N.; Poinssot, C.; Ravaux, J.; Brau, H. P. *Progress in Nuclear Energy* **2012**, *57*, 155.
- (11) Costin, D. T.; Mesbah, A.; Clavier, N.; Dacheux, N.; Poinssot, C.; Szenknect, S.; Ravaux, J. *Inorganic Chemistry* **2011**, *50*, 11117.
- (12) Labs, S.; Hennig, C.; Weiss, S.; Curtius, H.; Zanker, H.; Bosbach, D. *Environmental Science & Technology* **2014**, *48*, 854.
- (13) Boatner, L. A. In *Phosphates: Geochemical, Geobiological, and Materials Importance*; Kohn, M. J., Rakovan, J., Hughes, J. M., Eds.; Mineralogical Soc America: Washington, 2002; Vol. 48, p 87.
- (14) Ni, Y. X.; Hughes, J. M.; Mariano, A. N. *American Mineralogist* **1995**, *80*, 21.
- (15) Forster, H. J. *American Mineralogist* **1998**, *83*, 1302.
- (16) Rapp, R. P.; Watson, E. B. *Contributions to Mineralogy and Petrology* **1986**, *94*, 304.
- (17) Bowring, S. A.; Housh, T. *Science* **1995**, *269*, 1535.
- (18) Forster, H. J. *Lithos* **2006**, *88*, 35.
- (19) Bea, F. *Journal of Petrology* **1996**, *37*, 1601.
- (20) Franz, G.; Andrehs, G.; Rhede, D. *European Journal of Mineralogy* **1996**, *8*, 1097.
- (21) Heinrich, W.; Andrehs, G.; Franz, G. *Journal of Metamorphic Geology* **1997**, *15*, 3.
- (22) Buick, R.; Brauhart, C. W.; Morant, P.; Thornett, J. R.; Maniw, J. G.; Archibald, N. J.; Doepel, M. G.; Fletcher, I. R.; Pickard, A. L.; Smith, J. B.; Barley, M. E.; McNaughton, N. J.; Groves, D. I. *Precambrian Research* **2002**, *114*, 87.
- (23) Buick, R.; Thornett, J. R.; McNaughton, N. J.; Smith, J. B.; Barley, M. E.; Savage, M. *Nature* **1995**, *375*, 574.
- (24) Scharer, U.; Xu, R. H.; Allegre, C. J. *Earth and Planetary Science Letters* **1984**, *69*, 311.
- (25) Scharer, U. *Earth and Planetary Science Letters* **1984**, *67*, 191.
- (26) Bowring, S. A.; Erwin, D. H.; Jin, Y. G.; Martin, M. W.; Davidek, K.; Wang, W. *Science* **1998**, *280*, 1039.
- (27) Gibson, G. M.; Ireland, T. R. *Nature* **1995**, *375*, 479.
- (28) Seydoux-Guillaume, A. M.; Wirth, R.; Heinrich, W.; Montel, J. M. *European Journal of Mineralogy* **2002**, *14*, 869.
- (29) Rasmussen, B.; Fletcher, I. R.; Muhling, J. R.; Wilde, S. A. *Precambrian Research* **2010**, *180*, 26.
- (30) Rasmussen, B.; Fletcher, I. R.; Muhling, J. R. *Geochimica Et Cosmochimica Acta* **2007**, *71*, 670.
- (31) Montel, J. M.; Kornprobst, J.; Vielzeuf, D. *Journal of Metamorphic Geology* **2000**, *18*, 335.

- (32) Montel, J. M.; Razafimahatratra, D.; Ralison, B.; De Parseval, P.; Thibault, M.; Randranja, R. *European Journal of Mineralogy* **2011**, *23*, 745.
- (33) Andrehs, G.; Heinrich, W. *Chemical Geology* **1998**, *149*, 83.
- (34) Dacheux, N.; Clavier, N.; Podor, R. *American Mineralogist* **2013**, *98*, 833.
- (35) Schlenz, H.; Heuser, J.; Neumann, A.; Schmitz, S.; Bosbach, D. *Z Kristallogr* **2013**, *228*, 113.
- (36) Boatner, L.; Sales, B. In *Radioactive waste forms for the future*; Lutze, W., Ewing, R. C., Eds. 1988, p 495.
- (37) Terra, O.; Dacheux, N.; Audubert, F.; Podor, R. *Journal of Nuclear Materials* **2006**, *352*, 224.
- (38) Bregiroux, D.; Terra, O.; Audubert, F.; Dacheux, N.; Serin, V.; Podor, R.; Bernache-Assollant, D. *Inorganic Chemistry* **2007**, *46*, 10372.
- (39) Terra, O.; Dacheux, N.; Clavier, N.; Podor, R.; Audubert, F. *Journal of the American Ceramic Society* **2008**, *91*, 3673.
- (40) Oelkers, E. H.; Montel, J. M. *Elements* **2008**, *4*, 113.
- (41) Burakov, B. E.; Yagovkina, M. A.; Garbuzov, V. M.; Kitsay, A. A.; Zirlin, V. A. In *Scientific Basis for Nuclear Waste Management Xxviii*; Hanchar, J. M., StroesGascoyne, S., Browning, L., Eds. 2004; Vol. 824, p 219.
- (42) Ewing, R. C.; Lutze, W.; Weber, W. J. *J Mater Res* **1995**, *10*, 243.
- (43) Burghartz, M.; Matzke, H.; Leger, C.; Vambenepe, G.; Rome, M. *J Alloy Compd* **1998**, *271*, 544.
- (44) Foerster, H.-J. *American Mineralogist* **1998**, *83*, 259.
- (45) Podor, R.; Cuney, M.; Nguyen, T. C. *American Mineralogist* **1995**, *80*, 1261.
- (46) Forster, H. J.; Harlov, D. E. *Mineralogical Magazine* **1999**, *63*, 587.
- (47) Peiffert, C.; Cuney, M. *Journal of Conference Abstracts* **1999**, *4*, 522.
- (48) McCarthy, G. J.; White, W. B.; Pfoertsch, D. E. *Materials Research Bulletin* **1978**, *13*, 1239.
- (49) Harlov, D. E.; Wirth, R. *American Mineralogist* **2012**, *97*, 641.
- (50) Hanchar, J. M.; Finch, R. J.; Hoskin, P. W. O.; Watson, E. B.; Cherniak, D. J.; Mariano, A. N. *American Mineralogist* **2001**, *86*, 667.
- (51) Ledergerber, G.; Degueldre, C.; Heimgartner, P.; Pouchon, M. A.; Kasemeyer, U. *Progress in Nuclear Energy* **2001**, *38*, 301.
- (52) Recktenwald, G.; Deinert, M. *Energies* **2013**, *6*, 2291.
- (53) Dacheux, N.; Brandel, V.; Genet, M.; Bak, K.; Berthier, C. *New Journal of Chemistry* **1996**, *20*, 301.
- (54) Frondel, C.; Collette, R. L. *American Mineralogist* **1957**, *42*, 759.
- (55) Frontera, C.; Rodriguez-Carvajal, J. *Physica B: Condensed Matter* **2003**, *335*, 219.
- (56) Ravel, B.; Newville, M. *Journal of Synchrotron Radiation* **2005**, *12*, 537.
- (57) Ankudinov, A. L.; Ravel, B.; Rehr, J. J.; Conradson, S. D. *Physical Review B* **1998**, *58*, 7565.
- (58) Terra, O.; Clavier, N.; Dacheux, N.; Podor, R. *New Journal of Chemistry* **2003**, *27*, 957.
- (59) Mesbah, A.; Szenknect, S.; Clavier, N.; Lozano-Rodriguez, J.; Poinssot, C.; Den Auwer, C.; Ewing, R. C.; Dacheux, N. *Inorganic Chemistry* **2015**, *54*, 6687.
- (60) Taylor, M.; Ewing, R. C. *Transactions-American Geophysical Union* **1975**, *56*, 1076.
- (61) Milligan, W. O.; Mullica, D. F.; Beall, G. W.; Boatner, L. A. *Acta Crystallographica Section C* **1983**, *39*, 23.
- (62) Martins, J. L.; Zunger, A. *Physical Review B* **1984**, *30*, 6217.
- (63) Boyce, J. B.; Mikkelsen, J. C. *Physical Review B* **1985**, *31*, 6903.
- (64) Mikkelsen, J. C.; Boyce, J. B. *Physical Review B* **1983**, *28*, 7130.

- (65) Nästren, C.; Jardin, R.; Somers, J.; Walter, M.; Brendebach, B. *Journal of Solid State Chemistry* **2009**, *182*, 1.
- (66) Walter, M.; Somers, J.; Bouëxière, D.; Rothe, J. *Journal of Solid State Chemistry* **2011**, *184*, 911.
- (67) Begun, G. M.; Beall, G. W.; Boatner, L. A.; Gregor, W. J. *J Raman Spectrosc* **1981**, *11*, 273.
- (68) Syme, R. W. G.; Lockwood, D. J.; Kerr, H. J. *J Phys C Solid State* **1977**, *10*, 1335.
- (69) Kolesov, B. A.; Geiger, C. A.; Armbruster, T. *Eur J Mineral* **2001**, *13*, 939.
- (70) Poloznikova, M. E.; Fomichev, V. V. *Usp Khim+* **1994**, *63*, 419.
- (71) Strohhöfer, C.; Fick, J.; Vasconcelos, H. C.; Almeida, R. M. *J Non-Cryst Solids* **1998**, *226*, 182.
- (72) Yu, X. C.; Song, F.; Wang, W. T.; Luo, L. J.; Han, L.; Cheng, Z. Z.; Sun, T. Q.; Tian, J. G.; Pun, E. Y. B. *J Appl Phys* **2008**, *104*.
- (73) Hoskin, P. W. O.; Rodgers, K. A. *Eur J Sol State Inor* **1996**, *33*, 1111.
- (74) Geisler, T.; Burakov, B. E.; Zirlin, V.; Nikolaeva, L.; Poml, P. *Eur J Mineral* **2005**, *17*, 883.

Figure captions:

Figure 1. SEM micrographs of the $\text{Th}_{1-x}\text{Er}_x(\text{SiO}_4)_{1-x}(\text{PO}_4)_x$ solid solutions.

Figure 2. (a) PXRD patterns of the $\text{Th}_{1-x}\text{Er}_x(\text{SiO}_4)_{1-x}(\text{PO}_4)_x$ solid solution showing a shift towards to the low angles when increasing erbium loading. (b) Observed, calculated and the difference curves obtained during the Rietveld refinement of the PWRD pattern of the $x = 0.5$ sample.

Figure 3. General view of the zircon structure type down the c axis.

Figure 4. Evolution of the volume (\AA^3) in $\text{Th}_{1-x}\text{Er}_x(\text{SiO}_4)_{1-x}(\text{PO}_4)_x$ system.

Figure 5. Experimental $k^3\chi(k)$ EXAFS spectra of $\text{Th}_{1-x}\text{Er}_x(\text{SiO}_4)_{1-x}(\text{PO}_4)_x$ solid solutions and their respective Fourier Transform (FT) at the (a) Th L_3 -edge and (b) Er L_3 -edge. Coloured lines are the best fit achieved, black lines are the experimental data. FT peak positions are not corrected for phase shifts.

Figure 6. Interatomic distances Th-O (upper squares) and Er-O (bottom stars) vs composition in $\text{Th}_{1-x}\text{Er}_x(\text{SiO}_4)_{1-x}(\text{PO}_4)_x$ solid solutions. The square symbols represents the average value obtained by EXAFS.

Figure 7. Variation in the interatomic distances Th-Th(Er) (stars) and Er-Er(Th) (circles) vs composition in $\text{Th}_{1-x}\text{Er}_x(\text{SiO}_4)_{1-x}(\text{PO}_4)_x$ solid solutions.

Figure 8. Variation in the interatomic distances Th(Er)-Si(P) vs composition in $\text{Th}_{1-x}\text{Er}_x(\text{SiO}_4)_{1-x}(\text{PO}_4)_x$ solid solutions.

Figure 9. Raman spectra of the $\text{Th}_{1-x}\text{Er}_x(\text{SiO}_4)_{1-x}(\text{PO}_4)_x$ solid solutions in the $100\text{-}1500\text{ cm}^{-1}$ range.

Figure 10. Variation of the ν_1 vibration position versus x in the Raman spectra of the $\text{Th}_{1-x}\text{Er}_x(\text{SiO}_4)_{1-x}(\text{PO}_4)_x$ solid solutions.

Figure 11. FTIR spectra of the $\text{Th}_{1-x}\text{Er}_x(\text{SiO}_4)_{1-x}(\text{PO}_4)_x$ solid solutions in the $400\text{-}4000\text{ cm}^{-1}$ range, with focus on the $650\text{-}1200\text{ cm}^{-1}$ range showing the stretching modes of the XO_4 tetrahedrons.

Table1. EDX compositions determined for $\text{Th}_{1-x}\text{Er}_x(\text{SiO}_4)_{1-x}(\text{PO}_4)_x$ solid solutions.

x_{calc}	xEr	xTh	xP	xSi	Er+Th/Si+P
0.0	0	1	0	1	
0.1	0.12(1)	0.88(1)	0.05(2)	0.95(2)	1.1(1)
0.2	0.24(2)	0.76(2)	0.16(2)	0.84(2)	1.2(1)
0.3	0.36(1)	0.64(1)	0.27(1)	0.73(1)	1.2(1)
0.4	0.44(2)	0.56(2)	0.35(1)	0.65(1)	1.2(1)
0.5	0.56(3)	0.47(3)	0.45(1)	0.55(1)	1.2(1)
0.6	0.57(1)	0.43(1)	0.53(1)	0.47(1)	1.3(1)
0.7	0.75(3)	0.25(3)	0.70(1)	0.30(1)	1.2(1)
0.8	0.81(3)	0.19(3)	0.74(1)	0.26(1)	1.1(1)
0.9	0.89(1)	0.11(1)	0.86(1)	0.14(1)	1.1(1)
1.0	1	0	1	0	

1
2
3
4
5
6
7
8
9
10
11
12
13
14
15
16
17
18
19
20
21
22
23
24
25
26
27
28
29
30
31
32
33
34
35
36
37
38
39
40
41
42
43
44
45
46
47
48
49
50
51
52
53
54
55
56
57
58
59
60

Table 2. Refined unit cell parameters for the $\text{Th}_{1-x}\text{Er}_x(\text{SiO}_4)_{1-x}(\text{PO}_4)_x$ solid solution.

x_{calc}	a (Å)	c (Å)	Volume (Å ³)
0.0	7.1443(2)	6.3240(2)	322.79(1)
0.1	7.1177(1)	6.2882(1)	318.57(1)
0.2	7.1070(2)	6.2602(2)	316.20(2)
0.3	7.0761(3)	6.2321(3)	312.06(2)
0.4	7.0539(2)	6.1986(3)	308.43(2)
0.5	7.0361(3)	6.1627(3)	305.10(2)
0.6	7.0132(2)	6.1308(2)	301.55(1)
0.7	6.9943(2)	6.1004(2)	298.44(1)
0.8	6.9683(2)	6.0671(2)	294.61(1)
0.9	6.9288(3)	6.0401(3)	289.98(2)
1.0	6.8837(1)	6.0227(1)	285.39(1)

Table 3. Th_{1-x}Er_x(SiO₄)_{1-x}(PO₄)_x Fit results for the main coordination shells at the Th and Er L₃-edges

x	Th-O		Th--Si ₁		Th--Si ₂		Th--Th		
	R/ Å	σ ² / Å ²	R/ Å	σ ² / Å ²	R/ Å	σ ² / Å ²	R/ Å	σ ² / Å ²	
0	2.40 (8)	0.0058 (13)	3.20 (25)	0.0045 (36)	3.95 (36)	0.0077 (51)	3.93 (16)	0.0042 (18)	S ₀ ² =0.81 % R-factor=2.0 E ₀ =10.88
0.2	2.39 (6)	0.0057 (7)	3.18 (22)	0.0046 (29)	3.95 (26)	0.0061 (35)	3.92 (14)	0.0044 (15)	% R-factor= 1.1 E ₀ =10.16
0.3	2.40 (5)	0.0067 (8)	3.19 (25)	0.0050 (33)	3.95 (24)	0.0050 (32)	3.93 (17)	0.0056 (19)	% R-factor= 1.4 E ₀ =10.37
0.4	2.38 (7)	0.0049 (11)	3.19 (71)	0.0102 (12)	3.92 (39)	0.0045 (53)	3.90 (40)	0.0078 (50)	% R-factor= 2.8 E ₀ =10.37
0.5	2.38 (9)	0.0053 (8)	3.16 (26)	0.0033 (36)	3.93 (29)	0.0036 (37)	3.91 (37)	0.0084 (45)	% R-factor= 2.2 E ₀ =9.75
0.6	2.38 (9)	0.0069 (11)	3.17 (50)	0.0084 (80)	3.94 (25)	0.0018 (30)	3.90 (43)	0.0085 (45)	% R-factor= 2.9 E ₀ =9.75
0.7	2.39 (10)	0.0062 (11)	3.16 (22)	0.0022 (30)	3.95 (23)	0.0014 (27)	3.92 (35)	0.0080 (43)	% R-factor= 2.5 E ₀ =10.49
0.8	2.39 (9)	0.0060 (10)	3.16 (27)	0.0039 (39)	3.95 (21)	0.0010 (24)	3.90 (33)	0.0074 (39)	% R-factor= 2.1 E ₀ =10.47
	Er-O		Er--P ₁		Er--P ₂		Er--Er		
	R/ Å	σ ² / Å ²	R/ Å	σ ² / Å ²	R/ Å	σ ² / Å ²	R/ Å	σ ² / Å ²	
0									S ₀ ² =0.77
0.2	2.38 (14)	0.0111 (16)	3.08	0.0012	3.88	0.0101	3.94 (54)	0.0101	% R-factor= 4.4 E ₀ =15.47
0.3	2.36 (9)	0.0078 (10)	3.05 (29)	0.0073 (43)	3.83 (23)	0.0041 (14)	3.98 (16)	0.0041 (14)	% R-factor= 2.5 E ₀ = 14.69
0.4	2.35 (10)	0.0105 (12)	3.05 (25)	0.0040 (26)	3.84 (38)	0.0084 (38)	3.98 (40)	0.0084 (38)	% R-factor= 4.1 E ₀ = 14.28
0.5	2.36 (10)	0.0108 (14)	3.05 (33)	0.0088 (58)	3.83 (30)	0.0066 (23)	3.97 (24)	0.0066 (23)	% R-factor= 3.5 E ₀ =14.77
0.6	2.35 (10)	0.0086 (11)	3.06 (22)	0.0047 (35)	3.83 (42)	0.0102 (45)	3.96 (42)	0.0102 (45)	% R-factor= 3.2 E ₀ =14.40
0.7	2.36 (8)	0.0100 (10)	3.06 (22)	0.0067 (30)	3.85 (35)	0.0110 (36)	3.95 (34)	0.0110 (36)	% R-factor= 2.3 E ₀ = 15.00
0.8	2.35 (7)	0.0074 (9)	3.05 (24)	0.0070 (38)	3.89 (63)	0.0100 (35)	3.78 (62)	0.0100 (35)	% R-factor= 2.2 E ₀ = 14.74
0.9	2.35 (8)	0.0073 (9)	3.04 (18)	0.0036 (25)	3.89 (51)	0.0096 (26)	3.77 (53)	0.0096 (51)	% R-factor= 2.3 E ₀ = 15.02
1.0	2.34 (7)	0.0055 (8)	3.03 (16)	0.0018 (19)	3.88 (34)	0.0049 (11)	3.76 (22)	0.0049 (11)	% R-factor= 2.3 E ₀ =14.97

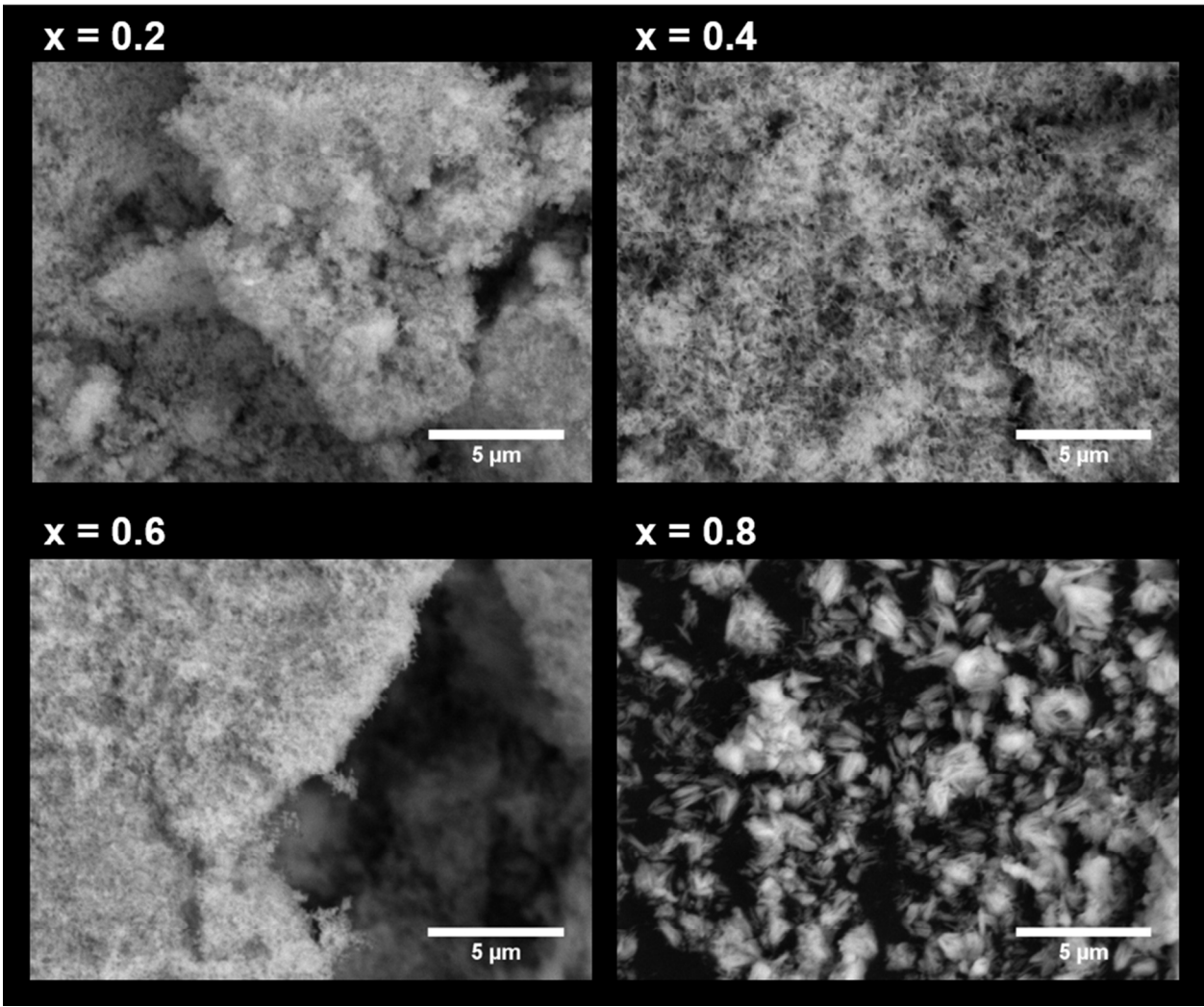


Figure 1. SEM micrographs of the $\text{Th}_{1-x}\text{Er}_x(\text{SiO}_4)_{1-x}(\text{PO}_4)_x$ solid solutions.

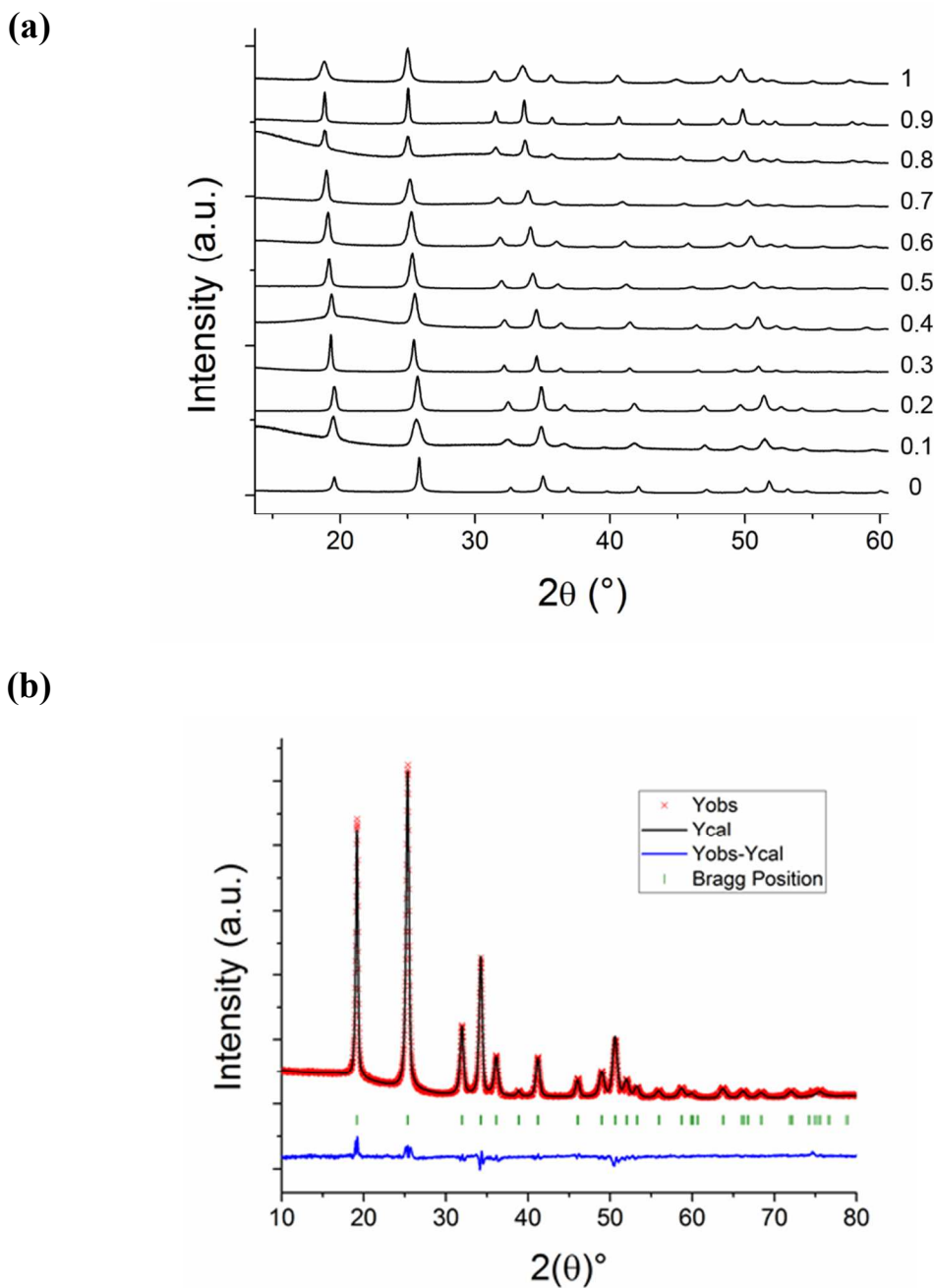


Figure 2. (a) PXRD patterns of the $\text{Th}_{1-x}\text{Er}_x(\text{SiO}_4)_{1-x}(\text{PO}_4)_x$ solid solution showing a shift towards the low angles when increasing erbium loading. (b) Observed, calculated and the difference curves obtained during the Rietveld refinement of the PWRD pattern of the $x = 0.5$ sample.

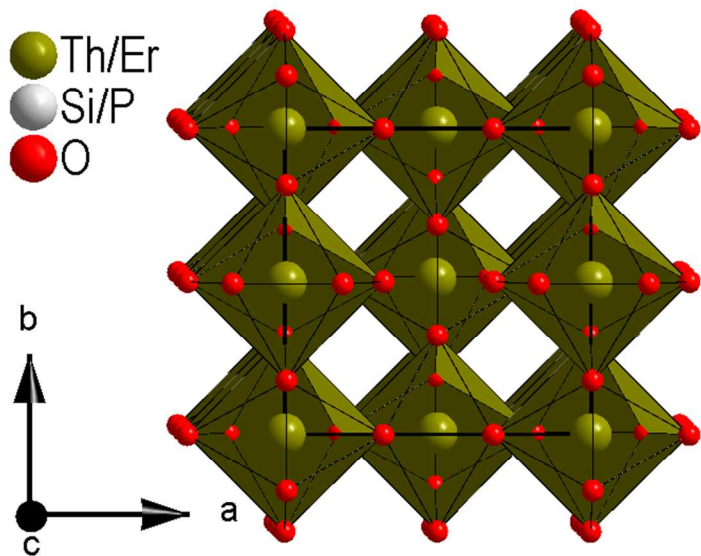


Figure 3. General view of the zircon structure type down the c axis.

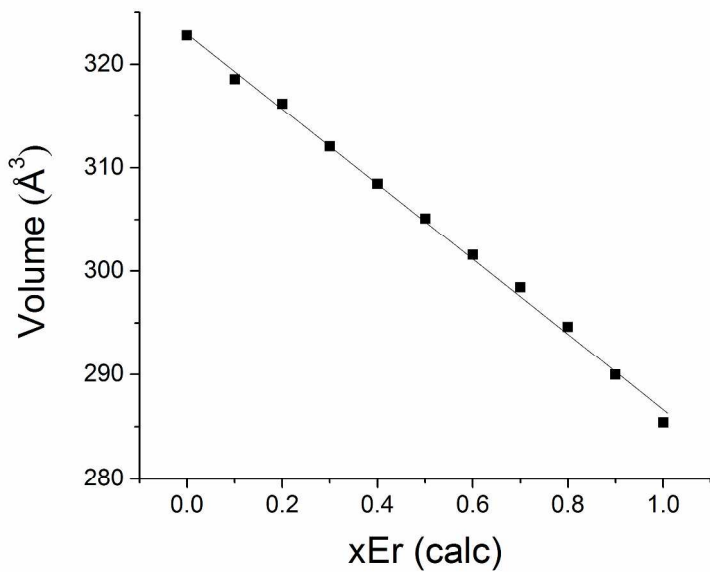


Figure 4. Evolution of the volume (Å³) in Th_{1-x}Er_x(SiO₄)_{1-x}(PO₄)_x system.

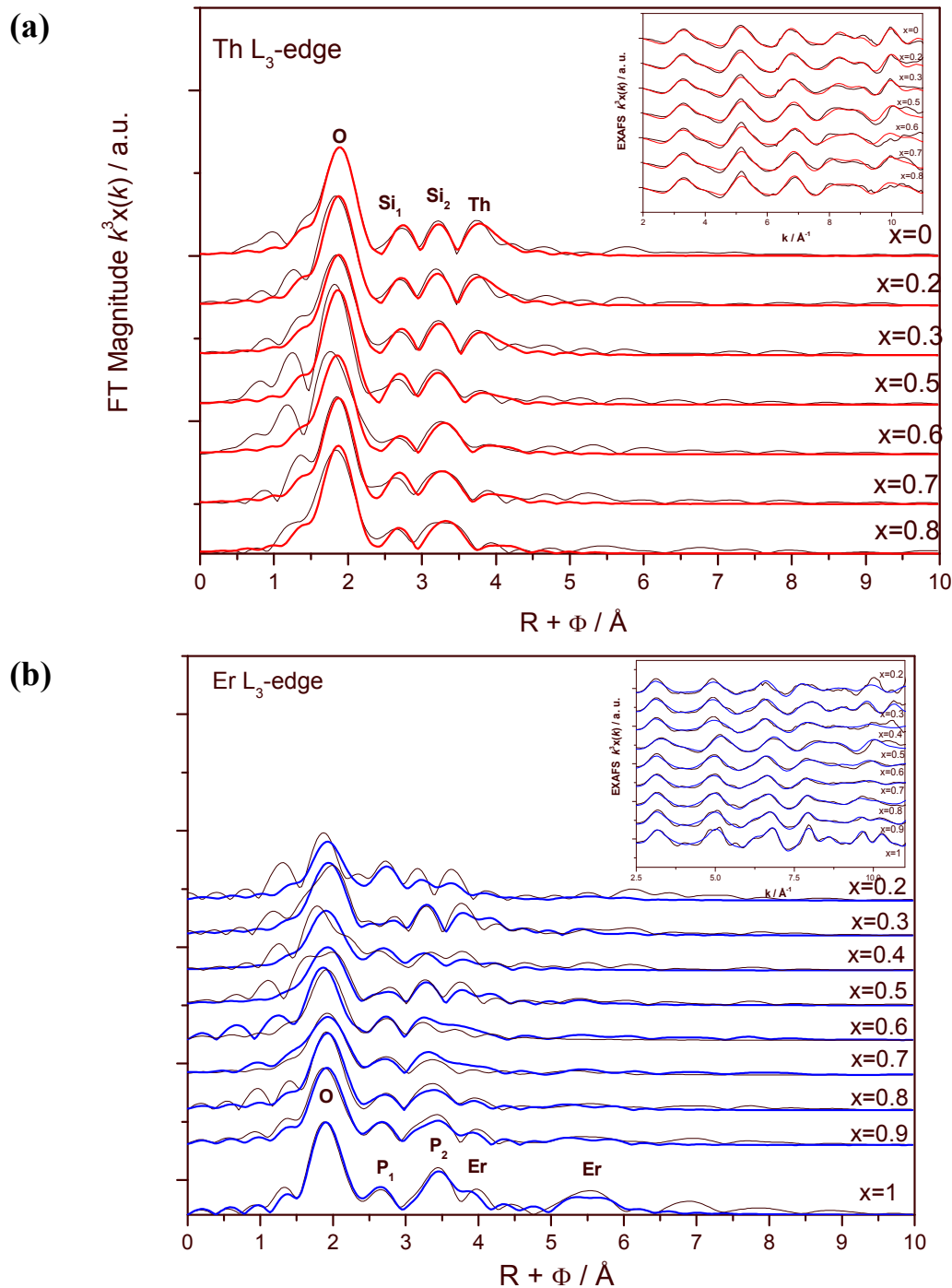


Figure 5. Experimental $k^3\chi(k)$ EXAFS spectra of $Th_{1-x}Er_x(SiO_4)_{1-x}(PO_4)_x$ solid solutions and their respective Fourier Transform (FT) at the (a) Th L_3 -edge and (b) Er L_3 -edge. Colored lines are the best fit achieved, black lines are the experimental data. FT peak positions are not corrected for phase shifts.

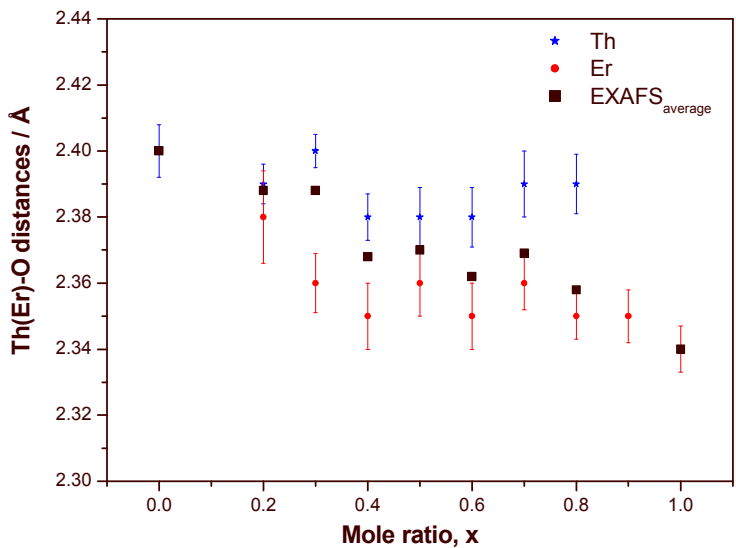


Figure 6. Interatomic distances Th-O (upper squares) and Er-O (bottom stars) vs composition in $\text{Th}_{1-x}\text{Er}_x(\text{SiO}_4)_{1-x}(\text{PO}_4)_x$ solid solutions. The square symbols represents the average value obtained by EXAFS.

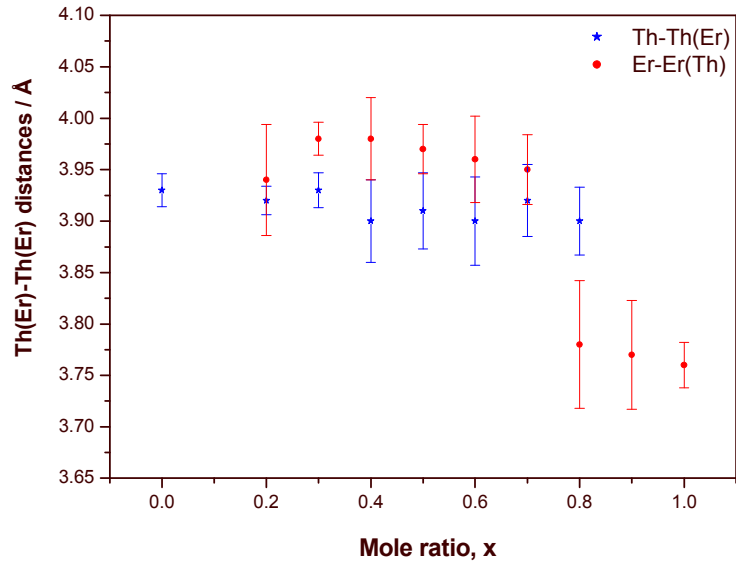


Figure 7. Variation in the interatomic distances Th-Th(Er) (stars) and Er-Er(Th) (circles) vs composition in $\text{Th}_{1-x}\text{Er}_x(\text{SiO}_4)_{1-x}(\text{PO}_4)_x$ solid solutions.

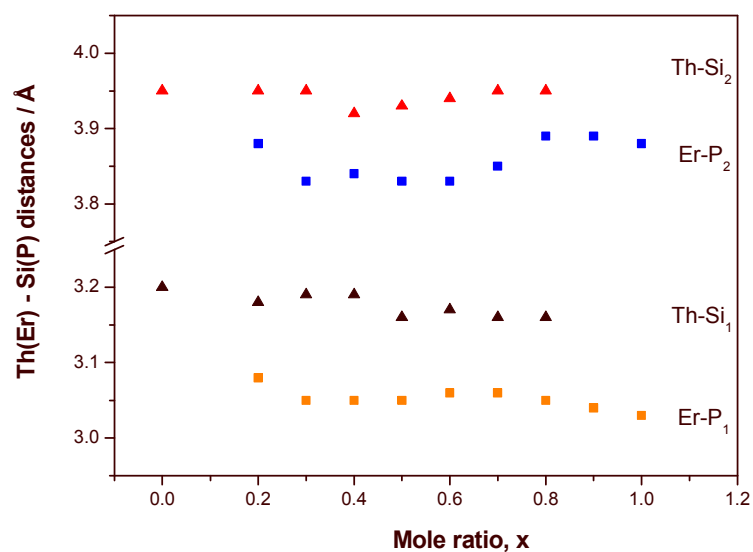


Figure 8. Variation in the interatomic distances Th(Er)-Si(P) vs composition in $\text{Th}_{1-x}\text{Er}_x(\text{SiO}_4)_1-x(\text{PO}_4)_x$ solid solutions.

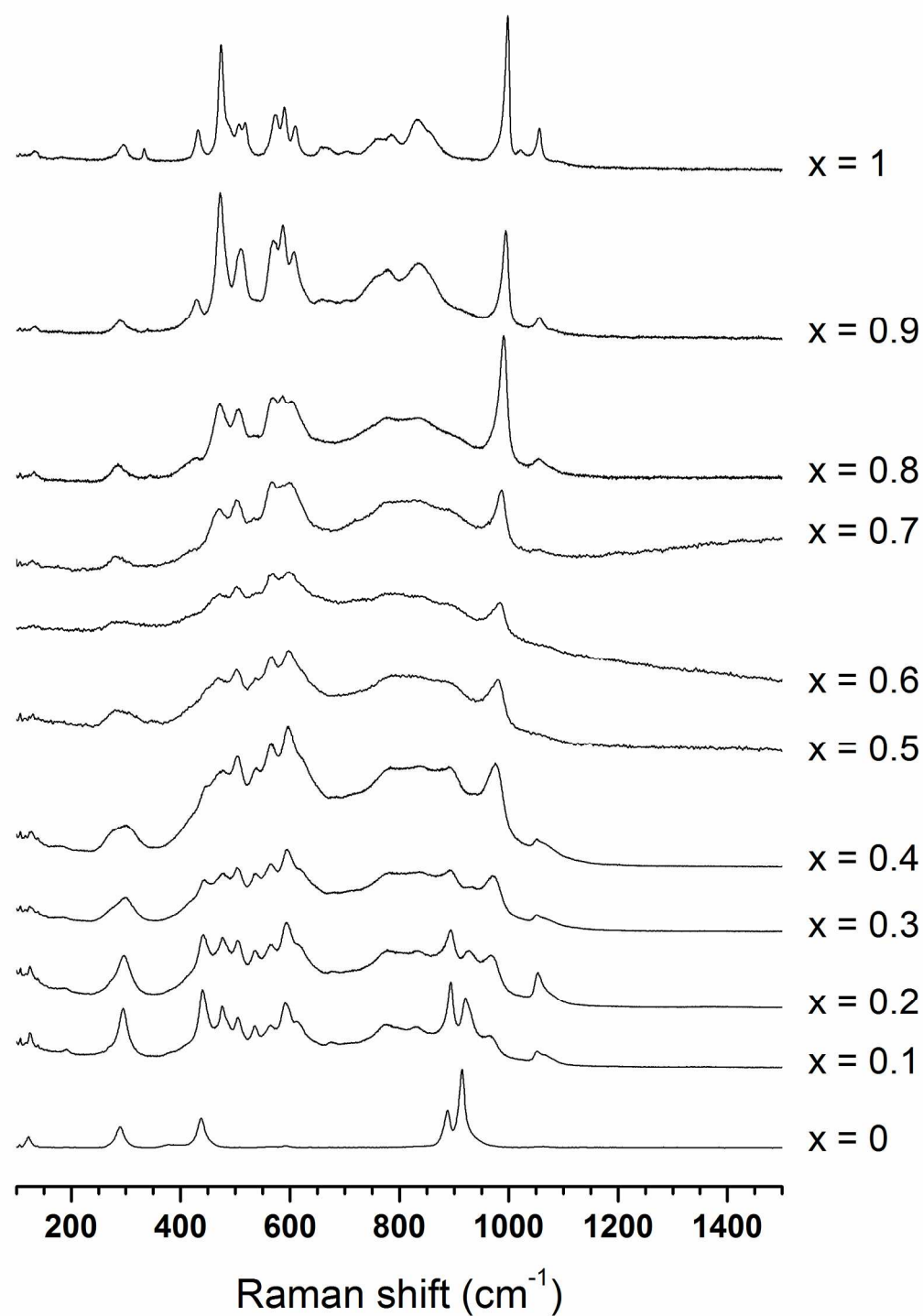


Figure 9. Raman spectra of the $\text{Th}_{1-x}\text{Er}_x(\text{SiO}_4)_{1-x}(\text{PO}_4)_x$ solid solutions in the 100-1500 cm^{-1} range.

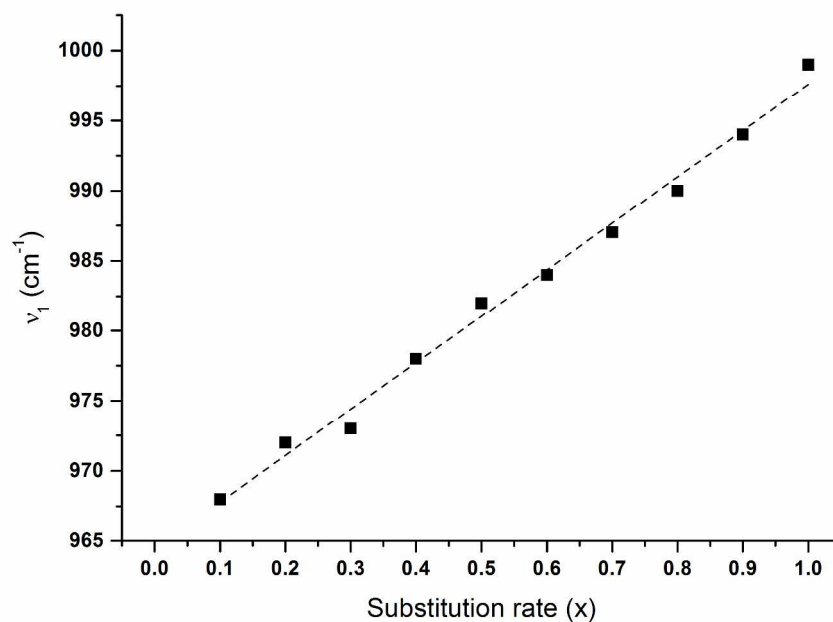


Figure 10. Variation of the ν_1 vibration position versus x in the Raman spectra of the $\text{Th}_{1-x}\text{Er}_x(\text{SiO}_4)_{1-x}(\text{PO}_4)_x$ solid solutions.

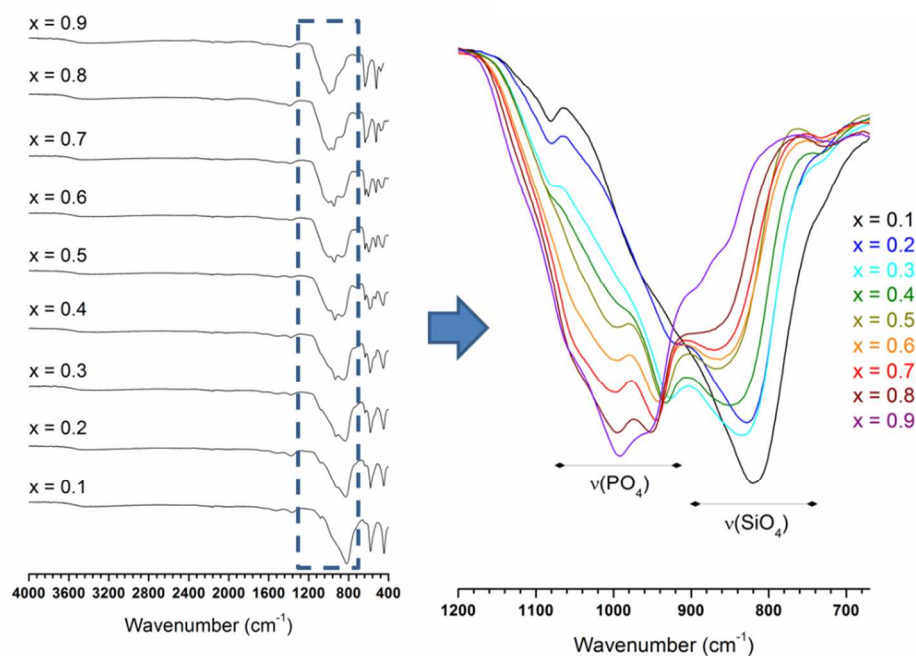


Figure 11. FTIR spectra of the $\text{Th}_{1-x}\text{Er}_x(\text{SiO}_4)_{1-x}(\text{PO}_4)_x$ solid solutions in the 400-4000 cm^{-1} range, with focus on the 650-1200 cm^{-1} range showing the stretching modes of the XO_4 tetrahedrons.

1
2
3
4
5
6
7
8
9
10
11
12
13
14
15
16
17
18
19
20
21
22
23
24
25
26
27
28
29
30
31
32
33
34
35
36
37
38
39
40
41
42
43
44
45
46
47
48
49
50
51
52
53
54
55
56
57
58
59
60

Synopsis

Pure $\text{Th}_{1-x}\text{Er}_x(\text{SiO}_4)_{1-x}(\text{PO}_4)_x$ compounds belonging to the zircon-xenotime family were synthesized under hydrothermal conditions (250°C, 7 days). PXRD, EDS, EXAFS, μ -Raman and FTIR analyses showed the formation of solid solution in agreement with the Vergard's law. The examination of the local structure shows that the Th-O distances remain close to those found in ThSiO_4 . Whereas, the Er-O distances show big decrease in function of erbium content and affects directly the PO_4^{3-} groups which are distorted.

